Elucidating the validity of electronic characteristics of transition metal perovskites as descriptors bridging electro- and chemocatalysis

Supporting Information

Sonja D. Mürtz[1] ‡, Johannes Simböck[1, 2] ‡, Feng Zeng[3, 1], M. Ghiasi[4], Simon Schönebaum[2,5], Ulrich Simon[2,5], Frank M.F. de Groot[4], Regina Palkovits[1, 2]*

[1]Chair of Heterogeneous Catalysis and Chemical Technology, RWTH Aachen University, Worringerweg 2, 52074 Aachen (Germany)

[2]Center for Automotive Catalytic Systems Aachen, RWTH Aachen University, Aachen, 52074 (Germany)

[3]State Key Laboratory of Materials-Oriented Chemical Engineering, College of Chemical Engineering, Nanjing Tech University, Nanjing, 211816 (China)

[4]Inorganic Chemistry and Catalysis, Debye Institute for Nanomaterials Science, Utrecht University, Universiteitsweg 99, 3584 CG Utrecht (Netherlands)

[5]Institute of Inorganic Chemistry, Landoltweg 1a, RWTH Aachen University, 52074 Aachen (Germany)

* Corresponding author: palkovits@itmc.rwth-aachen.de

‡ These two authors contributed equally to this work

Supplementary Note 1: Analysis of spin and oxidation states via Co L-edges

The electronic structure of the phase-pure perovskite-type oxides near the Fermi-level is generally dominated by contributions of O 2p as well as Co and Ni 3d states, in the catalysts at hand.[1,2] The non-TM cations La^{3+} [3], Al^{3+} [4] and Zn^{2+} [5] are of stable valence and do not contribute to the relevant density of states at this energy level.

The results of Co spin and oxidation state abundance revealed significant variation with composition and atmosphere during XAS experiments (Figure S1 and Table S1). Co^{3+} is partially reduced to Co^{2+} in materials with high Al substitution degree and LCZ-82 during UHV conditions. All materials are fully oxidized in O_2 presence. The spin state analysis showed that LS states are slightly more abundant in UHV compared to measurements in O_2 and that Zn and Al substitution leads to higher LS state abundance Ni remains trivalent throughout the measurements as shown in Ni L-edge measurements and occurs as stable LS configuration (Figure S1c). The average occupancy of t_{2g} and e_g orbitals was derived from abundance of the different Co spin and oxidation states, and Ni states for LCN-82, in the octahedral ligand field.

The analysis of the O K-edge (Supplementary Note 2, Figure S2) elucidated additional information on the hybridization of cationic states and O 2p states as it probes the electron density covalently transferred to TM (Co and Ni) 3d states. The transferred electron density from O 2p states to TM 3d is determined by integral quantification of the well-known spectral feature in the O K-edge.[6,7] The integrated area is normalized by several factors as described previously.[8] The normalization considers TM abundance in the material as well as t_{2g} and e_g occupancy of the TM states to yield a single-valued parameter, the covalency factor F_{cov}. The consideration of t_{2g} and e_g orbital occupancy in the normalization originates from the different orbital overlap of TM 3d with O 2p orbitals, which causes a different spectral contribution to the measured O K-edge. The covalency factor is a measure for the covalent electron density transfer from O 2p to TM 3d states. It thus describes the electron density at the catalytically active TM site and its ability to share electron density with the octahedral ligands, - and a reactant in case of surface sites. In addition, the combination of XPS valence band and O K-edge measurements and their placement on a common energy scale allowed to determine the charge-transfer energy, Δ_{CT} in the previous analysis, as they reflect the density of states above and below the Fermi-level[9]. (Supplementary Note 3 and Figure S3)

The thus determined electronic characteristics of Δ_{CT} and F_{cov} in the O 2p-Co 3d interaction vary significantly with catalyst composition as well as with XAS/XPS measurement conditions.

The respective correlations of covalency or charge-transfer energy with t_{2g} and e_g occupancy show significant scatter in UHV measurements. In contrast, the correlations in O_2 presence showed that both charge-transfer energy and covalency increase with t_{2g} occupancy and declined with e_g[10]. The definition of covalency as the ratio of overlap integral over charge-transfer energy[8] yields the conclusion that the overlap integral in the materials must increase pronouncedly upon substitution of Co with Al to warrant the measured changes in the electronic parameters. The cause of this increased overlap integral is the absence of relevant d-orbital states in Zn^{2+} and Al^{3+} and their lower electronegativity. These characteristics lead to an elevated electron density in the remaining Co-O substructure, which yields increased electron-electron repulsion and, thus, much more expansive orbitals with significantly pronounced overlap. The electron-electron repulsion also elevates the ligand field stabilization energy in the octahedral coordination. Together with a constant spin coupling energy this results in the measured higher LS abundance as well as more pronounced reducibility at high Al substitution degrees. In addition. the abundance of divalent cations (Co^{2+}, Zn^{2+}) is accompanied by the presence of oxygen vacancies, which was quantified from TM oxidation state abundance, assuming charge neutrality in the materials. Most catalysts were near-stoichiometric in their composition, the most pronounced non-stoichiometry was obtained for $LaCo_{0.8}Zn_{0.2}O_{3-\delta}$ with $\delta = 0.20$ (Table S1).

The electronic parameters of the catalysts, determined in the covalency factor, the charge-transfer energy, and the occupancy of t_{2g} and e_g states, thus, show a significant variation upon varied catalyst composition. The additional differences in electronic characteristics between the UHV and O_2 measurements enable to examine the potential impact of different oxidation and spin states on catalytic efficacy. The analysis of correlations between the catalytic rate and catalyst characteristics requires knowledge of further details of the reaction mechanism to determine relevant surface species and the kinetically relevant step of the reaction, which limits the overall reaction rate. Therefore, a mechanistic analysis of N_2O or NO reduction by CO is presented in the following before the correlations of catalytic rates and electronic characteristics are discussed.

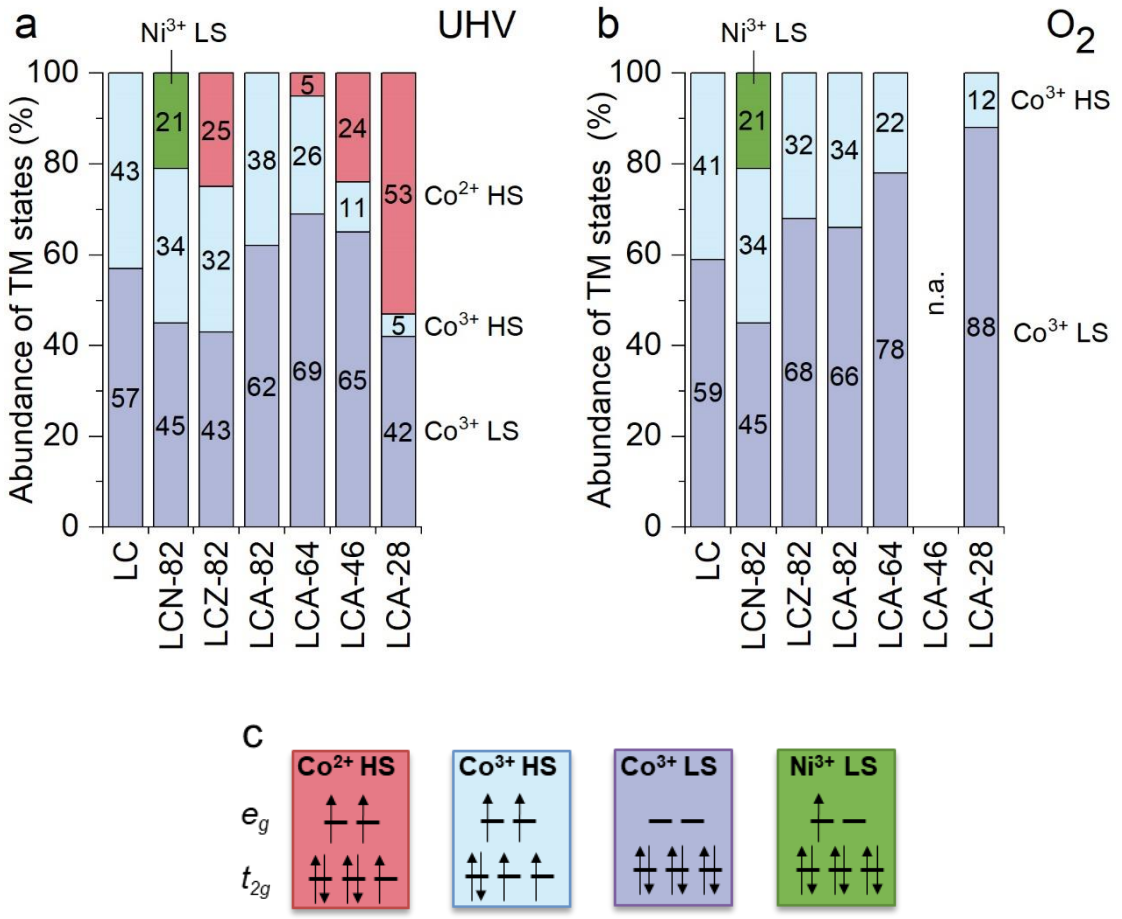

Figure S1 Abundance of transition metal oxidation and spin states. Abundance of transition metal (TM) states as derived from X-ray absorption spectroscopy at the Co $L_{2,3}$-edges at 623 K **a** in ultra-high vacuum (UHV) and **b** in 0.37 kPa O_2. **c** Electronic configuration of TM 3d orbitals of abundant, relevant electronic states. Spin states are denoted for high spin (HS) and low spin (LS) state. Reprinted with permission from ref.[10] under a Creative Commons Attribution 4.0 International License: http://creativecommons.org/licenses/by/4.0/.

Table S1: Comparison of different catalyst characteristiscs in UHV or in oxygen presence at 623 K. (HS = high spin).

	HS abundance/%		Co^{2+} abundance / %		Oxygen content*	
	UHV	0.37 kPa O_2	UHV	0.37 kPa O_2	UHV	0.37 kPa O_2
LC	43	41	< 5	0	2.98 -3.00	2.98 -3.00
LCZ	43	32	25	0	2.78	2.78
LCN	43	42	< 5	0	2.98 -3.00	2.98 -3.00
LCA-82	38	34	< 5	0	2.98 -3.00	2.98 -3.00
LCA-64	27	22	< 5	0	2.98 -3.00	2.98 -3.00
LCA-46	15	n.a.	24	n.a	2.88	2.88
LCA-28	11	12	53	0	2.74	2.74

*Values calculated based on charge neutrality and Co^{2+} abundance and Zn^{2+} content.

Supplementary Note 2: Analysis of O K-edge

The excitation of O 1s core electrons into O 2p states in O K-edge XAS quantifies O 2p states that are unoccupied because of hybridization of O 2p with cationic states. The three distinct features A, B and C in the O K-edge of LC (Figure S2) are dominated by O 2p-TM 3d hybridized states (~ 527-531 eV), O 2p-La 5d (~ 532-538 eV) and a mixture of O 2p-La 5d and O 2p-TM 4sp states (~ 539-548 eV), respectively[8]. The O K-edge of LC at 623 K in UHV is similar to previous literature reports[7], but changes significantly with substitution. Intensity of feature A decreases with substitution of Co^{3+} by Al^{3+} because the latter lacks relevant 3d states, while peak intensity of feature B increases due to the occurrence of Al 3p - O 2p hybridized states in this energy range[11].

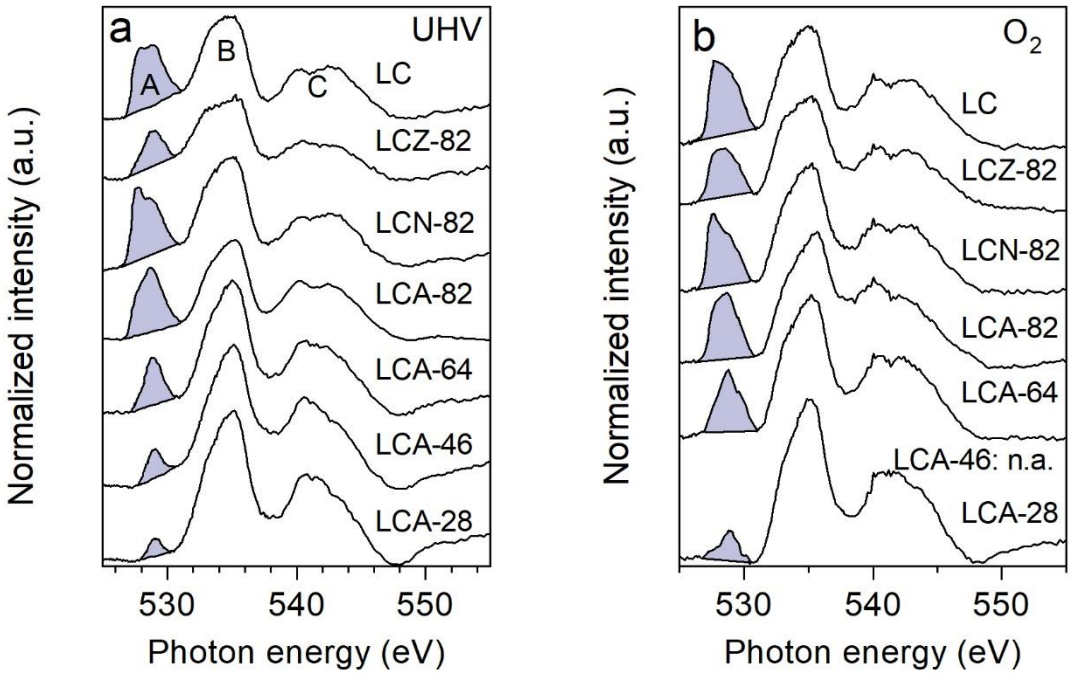

Figure S2 Analysis of O K-edge spectra. O K-edge of catalysts at 623 K **a** in UHV and **b** in 0.37 kPa O_2.

Supplementary Note 3: Determination of the charge-transfer energy Δ_{CT}

The analysis of the charge-transfer energy, $\Delta_{CT,}$ (Figure S3) requires alignment of the energies of XPS valence band and XAS O K-edge data on a common energy scale. A rigid shift of XAS energies is applied for this purpose and was chosen to equate to results for the charge-transfer energy Δ_{CT} of for $LaCoO_3$ in ref[9]. There, complementary DFT calculations and XES

measurements were applied to establish a valid analysis using XAS and XPS data. Values of Δ_{CT} shift systematically by the use of a rigid shift and allow a comparison among the oxides in this work. This approach assumes the premise that final state effects do not vary significantly among the oxides in this work.

Peaks in element specific XES measurements overlap well with XPS valence band peaks[9]. As a consequence, XPS valence band spectra and the peaks in it allow the analysis of electronic parameters, the charge-transfer energy Δ_{CT} for example. Most catalysts, including LC, show well-discernible double-peak feature in the valence band that relate to O 2p states[9]. When the peaks were not distinguishable, which is the case for LCZ-82 and LCA-28, the peak position of the non-bonding O feature was estimated at one third of the observed total breadth of the O 2p band. The energy difference from the peak center of the O K-edge, which relates to O 2p-TM 3d interaction, to the non-bonding O states in the XPS valence band yields the Δ_{CT} values.

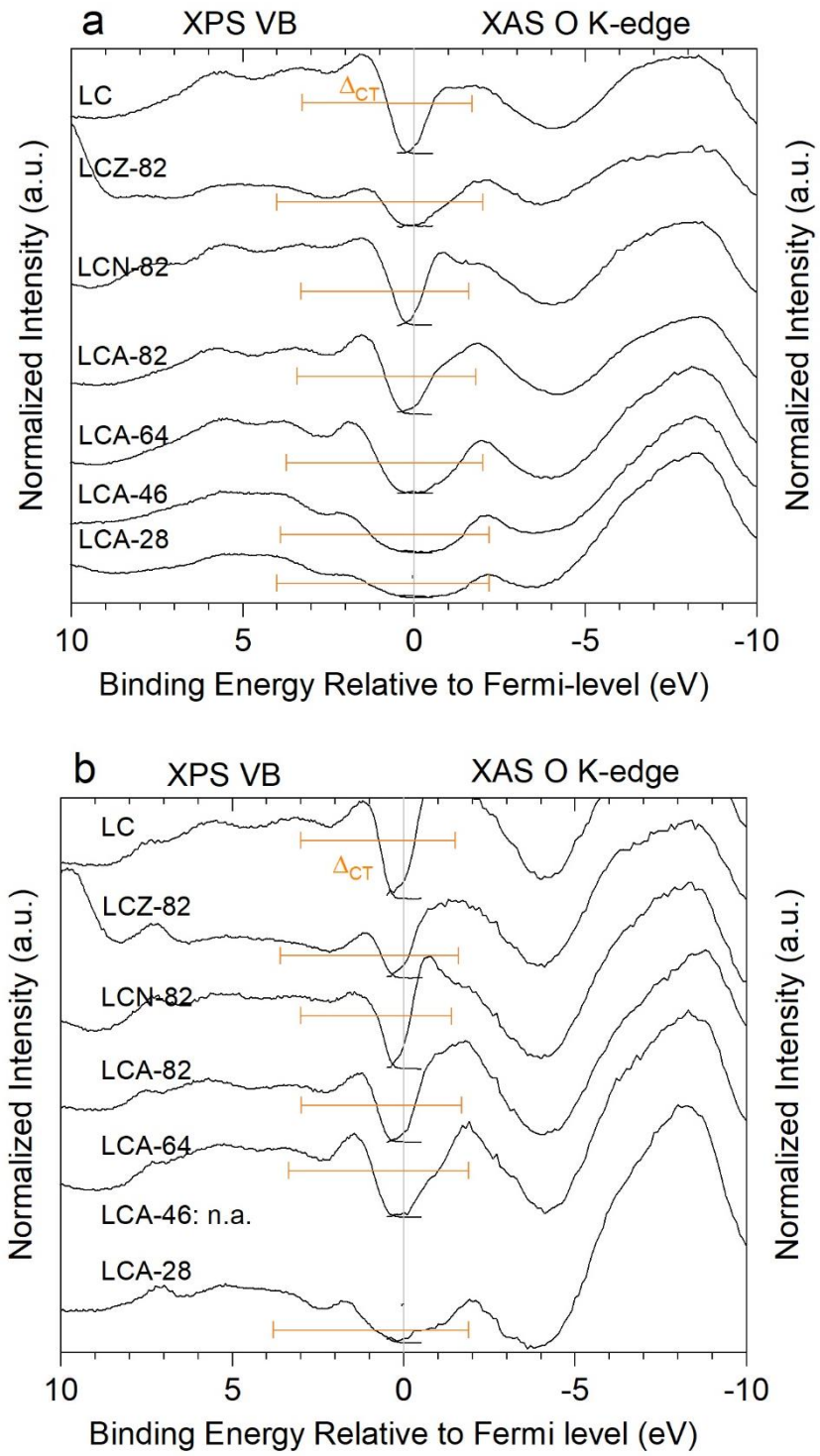

Figure S3 Determination of charge-transfer energy. Determination of charge-transfer energy (Δ_{CT}) at 623 K **a** in ultra-high vacuum (UHV) and **b** in 0.37 kPa O_2. XPS valence band data and XAS O K-edge data were normalized separately in arbitrary numbers. Absolute intensities are therefore not comparable.

Supplementary Note 4: Correlations of Electronic Parameters

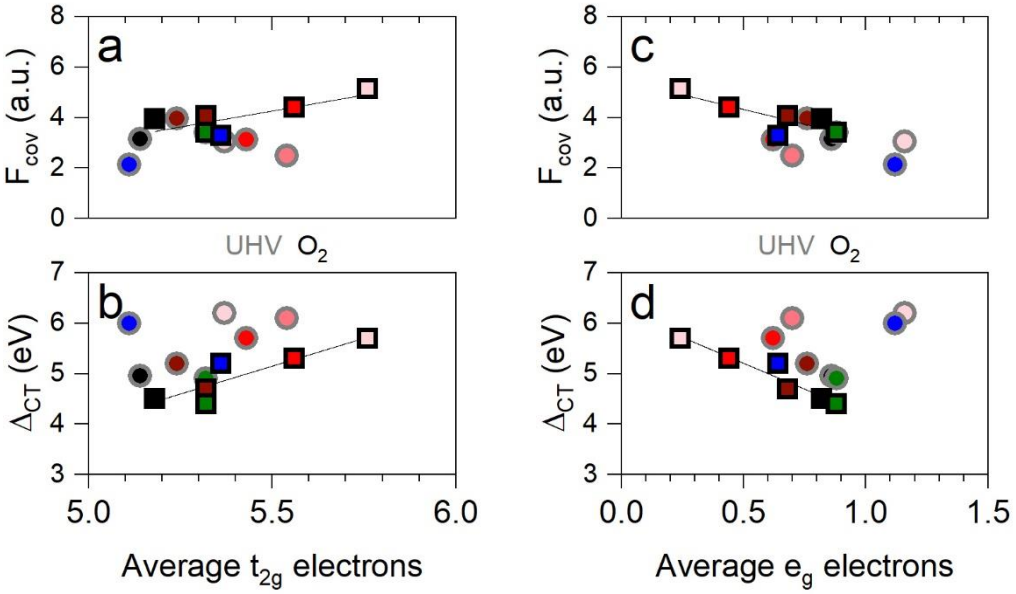

Figure S4 Intercorrelation of electronic parameters variation of charge-transfer energy (Δ_{CT}*) and covalency (F_{cov}) with occupancy of **a, b** transition metal (TM) t_{2g} or **c, d** TM e_g orbitals. Symbol edge color identifies F_{cov} in O_2 presence (black) or ultra-high vacuum (UHV, gray). Fill colors represent the substituent cation: Ni (green), Zn (blue), increasing Al fraction (dark to light red) and LC (black). Lines represent least squares fits of data measured in O_2 presence. *Please note that the charge-transfer gap was determined as the difference between energies of peak density of states for comparability to previous analysis (Supplementary Note 4). As a result true physical values are smaller than the reported values here. Reprinted with permission from ref [10] under a Creative Commons Attribution 4.0 International License: http://creativecommons.org/licenses/by/4.0/.

Supplementary Note 5: Effects of temperature on XAS measurements

It is important to note that XAS measurement temperatures of 623 K diverge from typical electrocatalysis conditions and that comparisons to previously reported data thus need careful consideration of this fact. While the differing measurement temperature affects the exact values of the descriptors, the correlation trend will only be influenced slightly. The conditions enable, however, a comparison of electro- and chemocatalytic data and the respective descriptors. The temperature difference does not affect oxidation states but spin state populations are vastly temperature-dependent. The Co low spin state (t_{2g}^6 e_g^0) becomes more prevalent relative to the high spin state (t_{2g}^4 e_g^2) with respective consequences for correlations with these parameters. However, all catalysts shift to the same direction, effectively leaving the correlations in place but in a narrower margin of e_g or t_{2g} occupancy. Measurements have shown that in the case of

LC the share of HS state reduces from 41 at 623 K to 29 % of Co 3d states at 423 K. Assuming a further reduction of HS state population may yield an estimated 25 % HS state population. LCA-82 shifts from 34 to 19 % respectively and LCN-82 and LCZ-82 likely shift similarly to LC. Analogously, covalency should shift concertedly among the set of catalysts, however, the complexity of the O 2p-TM 3d interaction renders this projection more fraught with uncertainty.

Supplementary Note 6: Effects of XAS atmosphere on the correlations

The e_g occupancy, covalency factor and charge transfer energy obtained in O_2 possess better correlation quality than the parameters acquired in UHV (Figure S7 and S8). The impact of XAS on the descriptor nature of the electronic characteristics is related to the state of surface sites of these oxides that are expected to be fully oxidized in KOH under OER and GOR conditions, and thus the electronic structure obtained in O_2 (fully oxidized Co) shows better correlation with electrocatalytic performance than the electronic structure obtained in UHV (partially reduced Co). The effect on correlations is particularly important with regard to catalyst treatment before XAS measurements. If such preparation includes burning off of carbon in the measurement chamber at elevated temperatures, a reduction of the catalyst is likely, which may complicate or hinder the use of the derived electronic characteristics as descriptors for electrocatalysis and chemocatalysis.

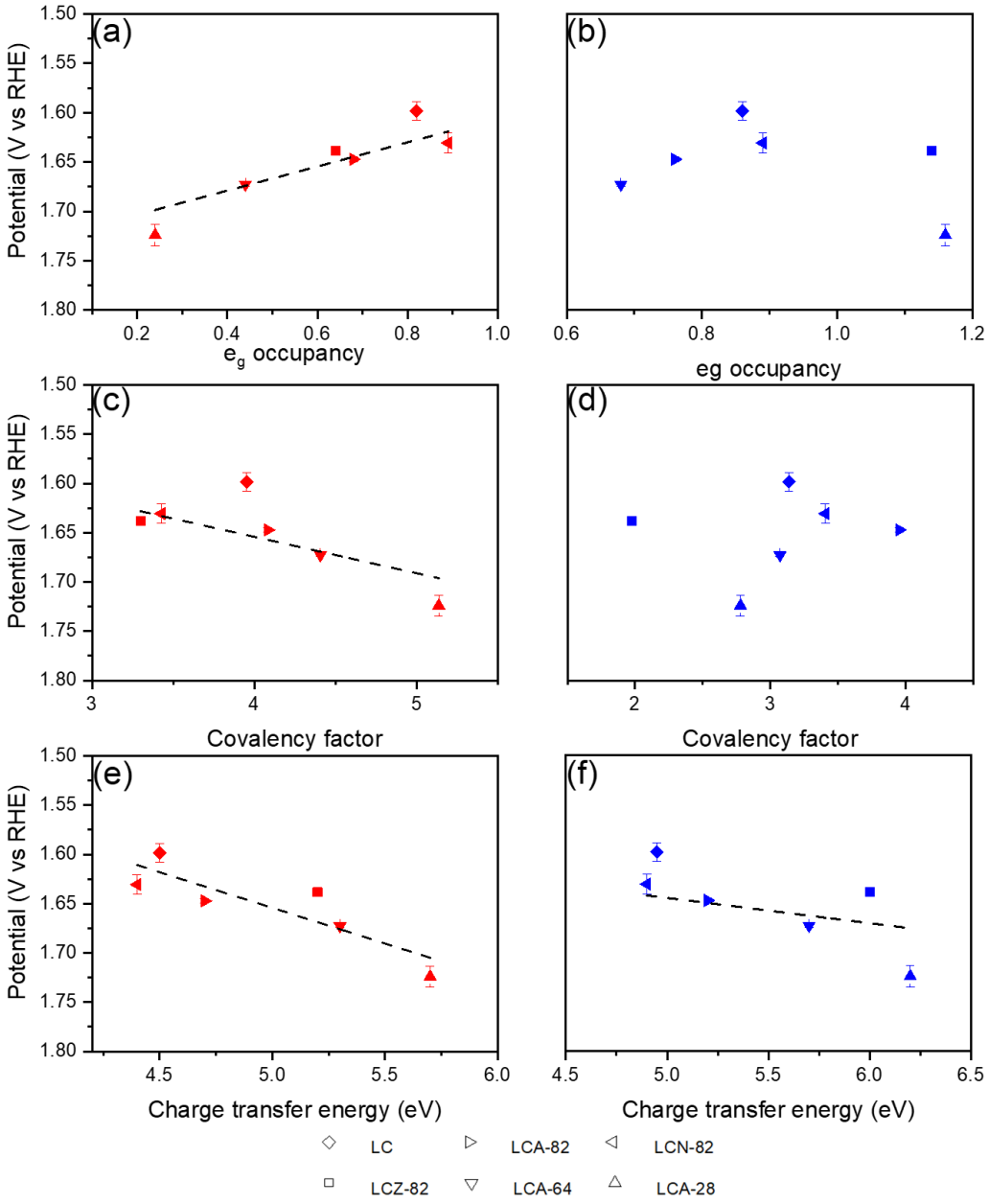

Figure S5 Correlations of electronic parameters in O_2 presence and UHV. The correlations of OER potential-e_g occupancy in O_2 presence (a) and UHV (b), OER potential-covalency factor in O_2 presence (c) and UHV (d), and OER potential-charge transfer energy in O_2 presence (e) and UHV(f).

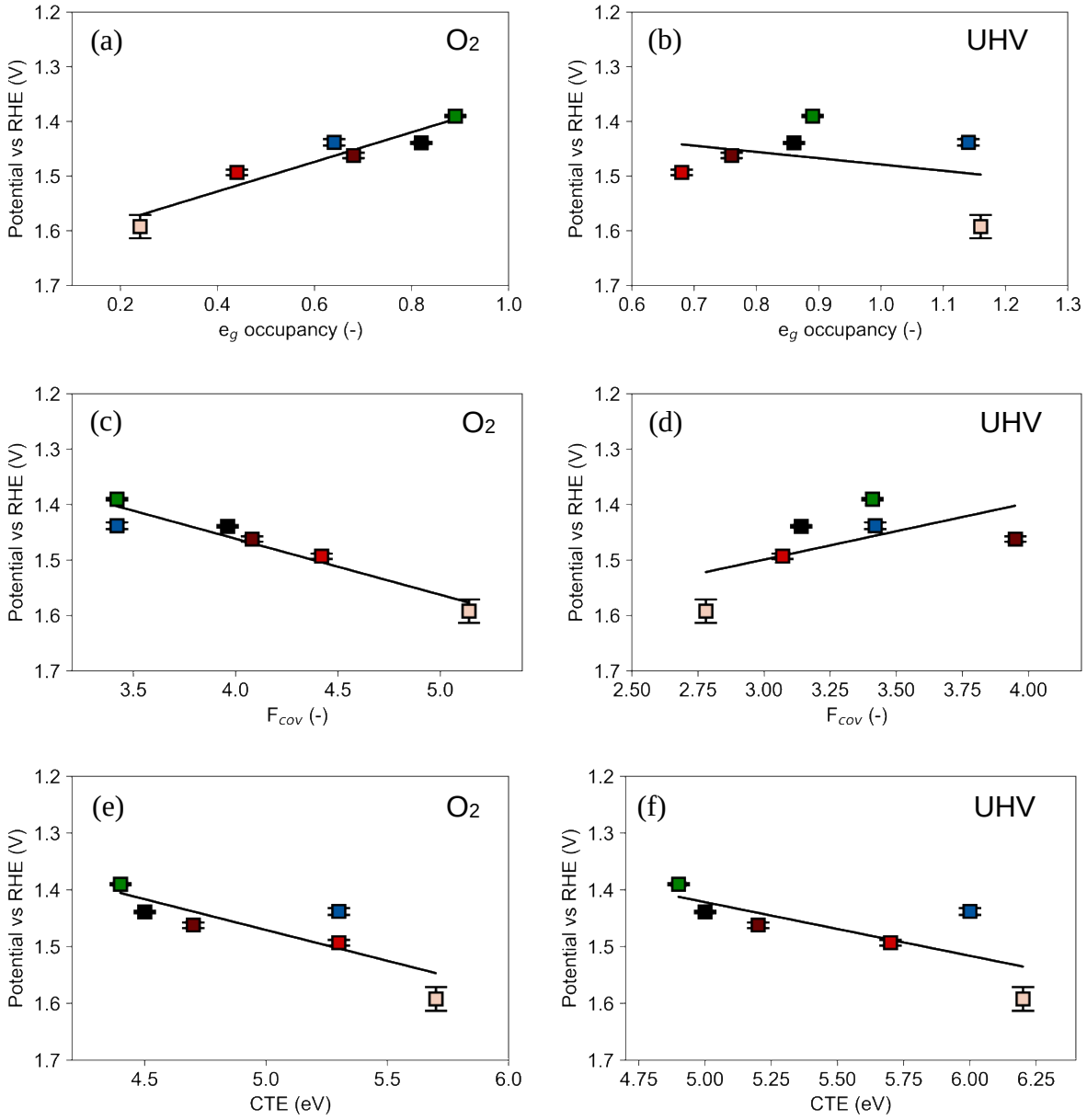

Figure S6 Comparison of correlations in O_2 presence and UHV. The correlations of GOR potential with e_g occupancy in O_2 presence (a) and UHV (b), GOR potential with covalency factor in O_2 presence (c) and UHV (d), and GOR potential-charge transfer energy in O_2 presence (e) and UHV(f). Ni (green), Zn (blue), increasing Al fraction (fading red fill) and LC (black). Lines represent least squares fits. The data and error were obtained based on three independent measurements.

Supplementary Note 7: Electrochemical Performance

We investigated the OER and GOR activity of the obtained materials in a typical three electrode cell in 1.0 M KOH and 1.0 M KOH with 1 M glycerol, respectively. Figure S5 presents the polarization curves, Tafel plots, and Nyquist plots of the OER normalized by the electrochemically active surface area (ECSA). The overpotential for OER on LC 0.37 V, which agrees well with literature values[7], is the smallest in the set of catalysts in this work. The overpotential increases slightly for all materials with low substitution degrees but increases significantly with Al substitution (Figure S5a) to a maximum value of 0.49 V for LCA-28. The Tafel slope values increase from 92 to 158 mV dec^{-1} in the same order, with the exception that LCN-82 shows the lowest value (Figure S1b). The results agree well with previous results on perovskite-type oxides where increasing Tafel slope values also indicated lower OER efficacy[12]. Results from electrochemical impedance spectroscopy (EIS) complement this analysis with data on OER kinetics as presented in Nyquist plots (Figure S5c). The EIS results were fit to an equivalent circuit to extract the charge transfer resistance (R_{ct}), which increases in the order of LCN-82 < LC < LCA-82 < LCZ-82 < LCA-64 < LCA-28 from 585 to 5954 ohm. The increase in R_{ct} among the catalysts is in close correlation with OER efficacy, underlining the increasing electron transfer barrier with substitution.

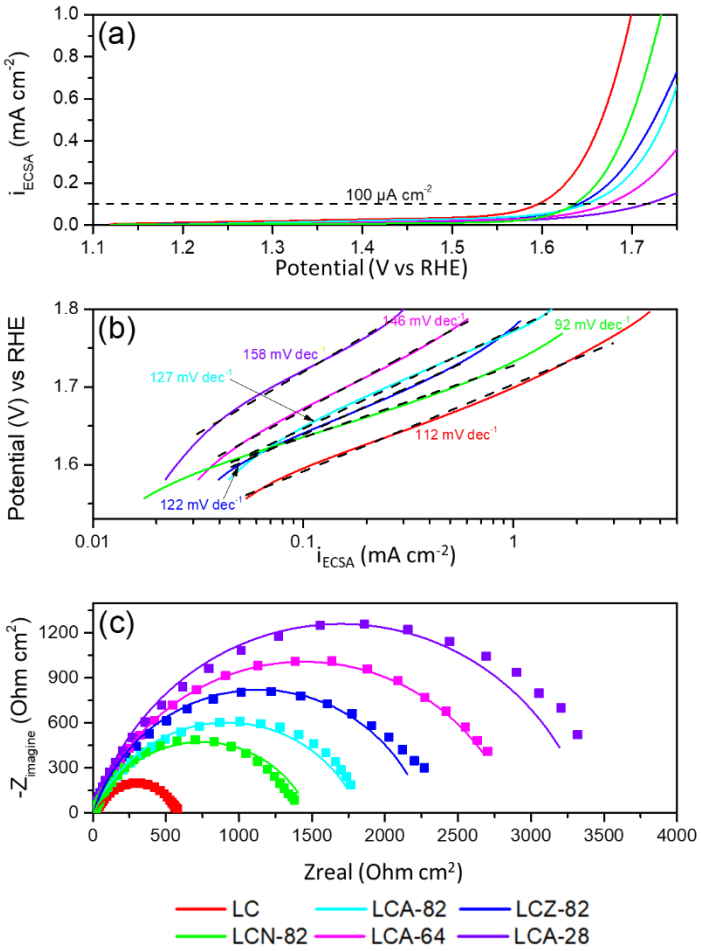

Figure S7 Polarization curves (a), Tafel plots (b), and Nyquist plots (c) of the $LaCoO_3$ derivatives. The dash lines in (b) and solid lines in (c) are the fitting results. All the measurements were performed in 1.0 M KOH; rotating speed, 2500 rpm; catalyst loading, 109 µg cm^{-2}. The results presented here are the medium value of three independent measurements.

Figure S6 depicts the polarization curves, Tafel plots, and Nyquist plots of the GOR normalized by ECSA. The potential for GOR at 100 µA cm^{-2} for LC is 1.44 V vs RHE, which is lower than for OER demonstrating the potential as an alternative anode reaction in hydrogen production. The potential increases significantly with Al substitution to a maximum value of 1.59 V vs RHE for LCA-28. The lowest potential of 1.38 V vs RHE is obtained on LCN, which was already reported as a good catalyst for GOR in literature[13]. The Tafel slope values increase from 105 to 169 mV dec^{-1} with increasing aluminum content. The results combined with the OER data clearly underline that increasing Tafel slope values lead to lower efficacy as a result of a higher barrier for electron transfer. The Nyquist plots present the results from electrochemical impedance spectroscopy (EIS) which complement this analysis with data on GOR kinetics. The charge transfer resistance (R_{ct}) increases in the order of LCN-82 < LC < LCA-82 < LCZ-82 < LCA-64 < LCA-28 from 63 to 7897 ohm underlining again the increasing electron transfer barrier with substitution.

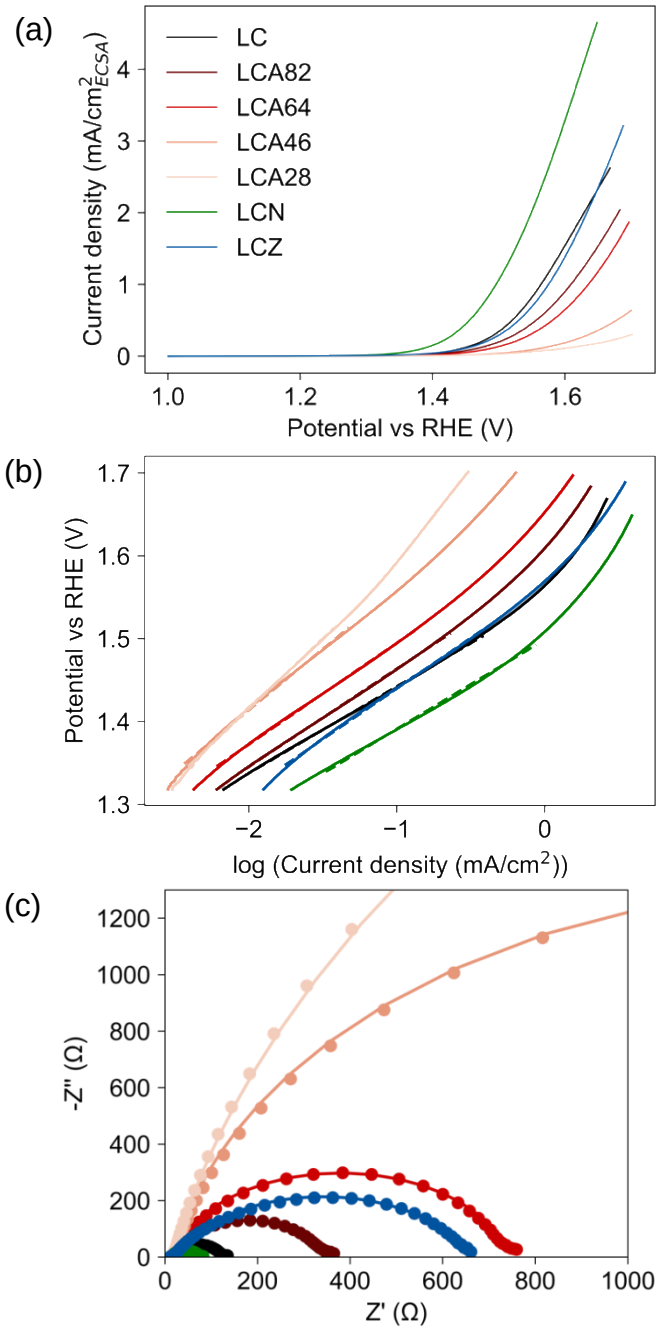

Figure S8 Polarization curves (a), Tafel plots (b), and Nyquist plots (c) of the $LaCoO_3$ derivatives. The dash lines in (b) and solid lines in (c) are the fitting results. All the measurements were performed in 1.0 M glycerol in 1.0 M KOH; rotating speed, 1200 rpm; catalyst loading, 190 μg cm^{-2}. The results presented here are the medium value of three independent measurements.

Supplementary Note 8: Correlations of Tafel slope and charge transfer resistance with e_g occupancy, covalency factor and charge transfer energy

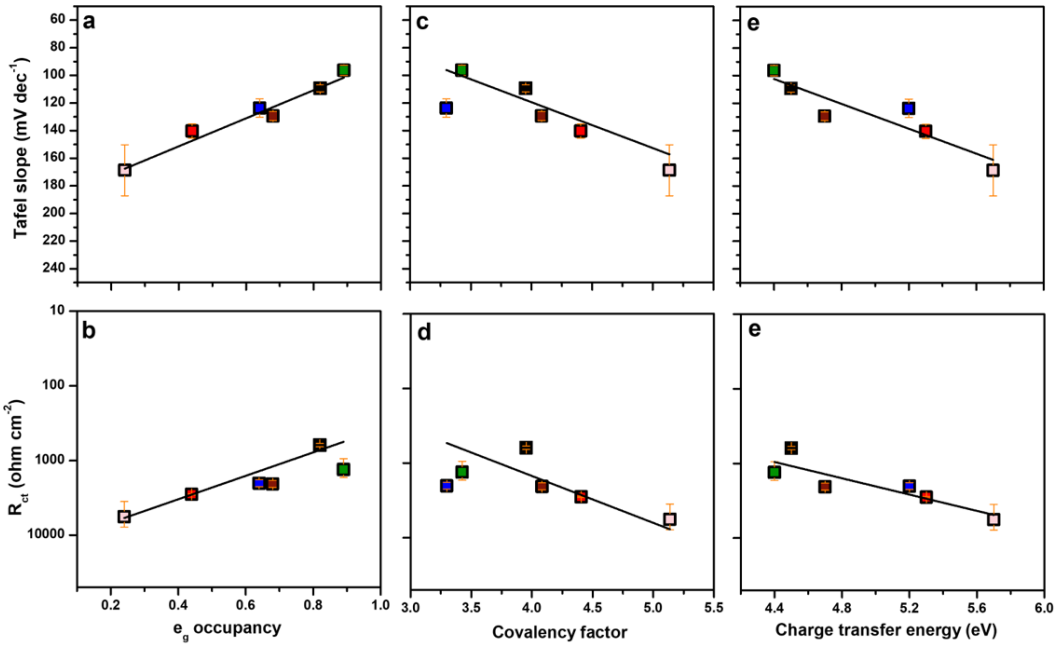

Figure S9 The correlations between OER Tafel slope and charge transfer resistance with the e_g occupancy (a, b), covalency factor (c, d) and the charge transfer energy (e, f), respectively. Ni (green), Zn (blue), increasing Al fraction (fading red fill) and LC (black). Lines represent least squares fits. The data and error were obtained based on 3 independent measurements.

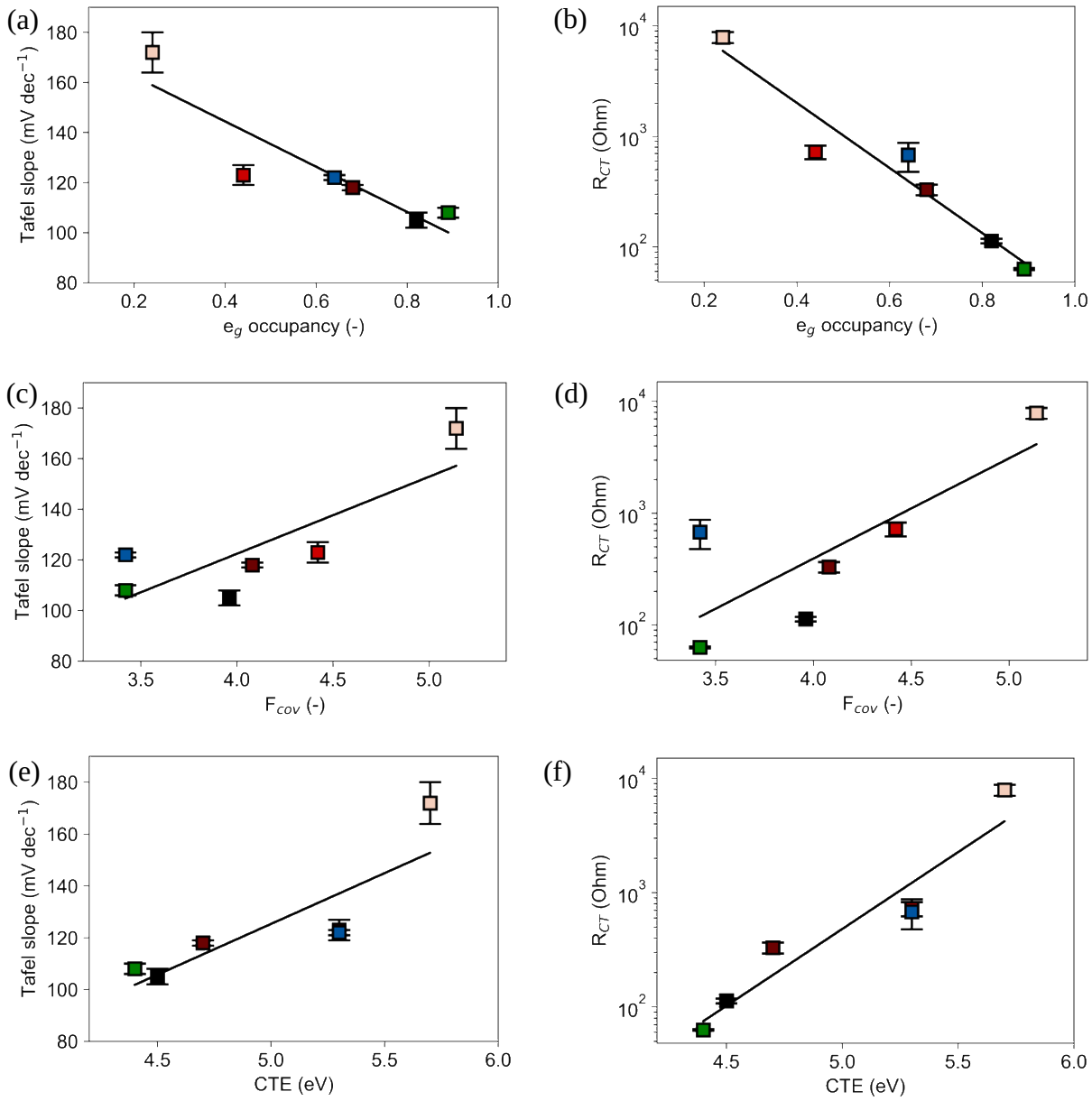

Figure S10 The correlations between GOR Tafel slope and charge transfer resistance with the e_g occupancy (a, b), covalency factor (c, d) and the charge transfer energy (e, f) in O_2 presence, respectively. Ni (green), Zn (blue), increasing Al fraction (fading red fill) and LC (black). Lines represent least squares fits. The data and error were obtained based on three independent measurements.

Supplementary Note 9: Reaction mechanism for OER

Suntivich et al.[14] proposed that OER over perovskite can be rate limited either by the formation of the O-O bond in OOH adsorbate ($B^{(m+1)+}$-O^{2-} + OH^- → $B^{(m)+}$-OOH^- + e^-, step 2) or the deprotonation of the oxyhydroxide group to form peroxide ions ($B^{(m)+}$-OOH^- + OH^- → $B^{(m+1)+}$-O_2^{2-} + H_2O + e^-, step 3). If a catalyst is located on the left branch of e_g occupancy-OER activity plot, step 3 is the rate determining step, and otherwise, step 2 is the rate determining step. All of our catalysts are located on the left branch indicating the deprotonation of the oxyhydroxide group to form peroxide ions is the rate determining step with the oxidation of B site metal to a higher oxidation state. More specifically, this rate determining step, a proton-coupled electron transfer (PCET), can proceed concertedly or in series (Figure S11)[15]. As the charge-transfer energy increases, the proton and electron transfer is decoupled, and the reaction becomes limited by the electron-transfer elementary step because the barrier to proton transfer becomes energetically more favorable[15,16]. Thus, the rate of electron-transfer determines the overpotential for all catalysts examined in this study.

The OER mechanisms may change with increasing covalency. At low covalency, the surface metal governs the OER, while at higher covalency the oxidation of lattice oxygen is involved in OER[15,17,18]. The kinetically relevant step may shift from O-O bond formation to the deprotonation of surface hydroxyl groups with increasing Co-O covalency. It is also proved that at low covalency proton and electron are transferred concertedly, while at high covalency decoupled proton-electron transfer occurs.[15] Thus OER over the $LaCoO_3$ derivatives may involve the oxidation of the surface oxygen, and the further increasing covalency leads to decreasing OER activity due to the degradation of the materials. In this case, the RDS, deprotonation of hydroxyl groups, become non-concerted.

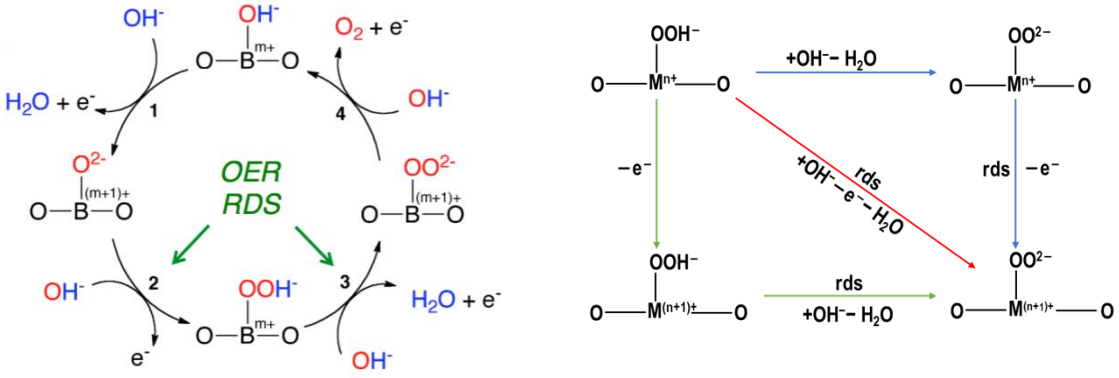

Figure S11 OER Reaction mechanism. Reprinted with permission from Suntivich et al.

Supplementary Note 10: Experimental procedure for electrochemical measurements

Electrochemical measurements were performed on an Autolab PGSTAT 302 N electrochemical workstation connected to a three-electrode cell with a glassy carbon rotating disc as the working electrode, an Ag/AgCl electrode as the reference electrode, and a glassy carbon rod as the counter electrode. For OER experiments, the catalyst suspensions with a concentration of 5.5 mg/mL (5.0 mg/mL for GOR) in Nafion solution (2 v% Nafion solution (5%, Aldrich), 49 v% H_2O, and 49 v% ethanol) were treated in an ultrasonic bath to obtain a well dispersed ink. Then 2.5 μL (9.4 μL for GOR) ink were dropped on the working electrode to obtain a catalyst loading of 109 μg cm^{-2} (190 μg cm^{-2} for GOR). The electrochemical measurements were carried out in a 1.0 M KOH solution (pH=14) at room temperature with a rotating speed of 2500 rpm (1200 rpm for GOR). The polarization curve was collected by a cyclic voltammetry (CV) scan (5 mV s^{-1}, 1.11-1.86 V vs RHE (OER), 1.0-1.7 V versus RHE (GOR)) after stabilization with 100 CV scans (1.11-1.71 V vs RHE, 100 mV s^{-1}) for OER and 25 CV scans (1.0 - 1.4 V vs RHE, 100 mV s^{-1}) for GOR. Double layer capacitances (C_{dl}) and electrochemically active surface area (ECSA) were obtained by CV measurements with different scan rate in a non-faradaic potential range. Electrochemical impedance spectroscopy (EIS) was conducted over a frequency range of 100 kHz to 50 mHz at 1.61 V versus RHE (for GOR: 100 kHz to 10 mHz at 1.6 V versus RHE) with an amplitude of the sinusoidal voltage perturbation of 10 mV. The charge transfer resistance was extracted by fitting the EIS result with an equivalent circuit as shown in Figure S5 and S6. All the catalysts were tested three times to obtain the mean and error of the electrochemical performance. The potentials were corrected with IR compensation to RHE by the formula V_{RHE} (V) = $V_{Ag/AgCl}$ + 0.21 + 0.059 × pH – I × R_s.

The ECSA was calculated by the following formula,

$$\mathrm{ECSA} = \frac{C_{dl}}{C_s} \times S_{geo}$$

C_s is the capacitance of a smooth planar surface, C_s=0.040 mF cm^{-2} is used for calculation.[19] S_{geo} is geometric surface area of the electrode (0.126 cm^2). C_{dl} is the double layer capacitance and is extracted from the CV under different scan rates in the non-faradaic potential range according to Morales[20] (0.85 – 1.2 V vs RHE, 0.02 - 0.16 V/s for OER, 0.01 – 1 V/s for GOR). The current density and EIS results were normalized by ECSA.

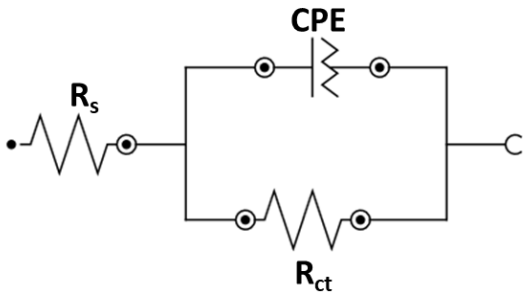

Figure S12 Equivalent circuit for EIS fitting. R_s is the serial resistance. R_{ct} is the charge transfer resistance. CPE is the constant phase element related to the double layer capacitance.

Supplementary Note 11: Reaction mechanisms of N2O or NO reduction by CO

The reduction reactions of NO or N_2O by CO each represent the abatement of two undesired combustion products. The mechanism of N_2O reduction by CO is addressed first because it may be a subset of the NO + CO reaction, where N_2O is formed and thus affects selectivity considerations.

N_2O + CO Reaction

The reduction reactions of NO or N_2O by CO each represent the abatement of two undesired combustion products. The reduction of N_2O selectively yields the products N_2 and CO_2, while the NO + CO reaction may lead to the formation of N_2 or N_2O as well as CO_2[21]. The selectivity pathways require careful consideration because the calculation of NO reaction rates need to account only for NO molecules that are activated in the kinetically relevant step – disregarding adsorbed NO molecules that react in another, faster reaction step of the same pathway, in a reaction of N* + NO* for example. The impact of other reaction steps from N_2O decomposition is insignificant because reaction temperatures were below the threshold of N_2O decomposition activity in tests of the same catalysts[10]. The mechanism of N_2O reduction by CO is addressed first because it may be a subset of the NO + CO reaction, where N_2O is formed and thus affects selectivity considerations.

The literature on the mechanism of the N_2O + CO reaction on perovskite-type oxides is limited both in scope and abundance. Mechanistic considerations on Co-Mn-Al oxides acknowledged the activation of N_2O as kinetically relevant step[22]. Different pathways of N_2O activation in presence of CO are described in literature on varying Co-based TM oxides[22–24], the elementary steps are shown in Scheme S1: The activation of N_2O may occur through the decomposition of adsorbed N_2O, where N_2O adsorbs on free active sites that originate from a fast surface reaction of CO* + O* or in a bimolecular mechanism of a concerted N_2O-CO reaction step. CO assists in the scission of the N-O bond of N_2O in a surface reaction or alternatively in an Eley-Rideal-type mechanism, where N_2O remains in the gas phase.

$$CO + * \rightleftharpoons CO* \quad (1)$$

$$N_2O + * \rightleftharpoons N_2O* \quad (2)$$

$$CO^* + N_2O^* \xrightarrow{} N_2 + CO_2^* + * \quad (3)$$

$$CO^* + N_2O \xrightarrow{} N_2 + CO_2^* \quad (4)$$

$$CO_2^* \rightleftarrows CO_2 + * \quad (5)$$

Scheme S1 Elementary steps of the N_2O + CO reaction. The arrow $\rightleftarrows$ signals the quasi-equilibration of the reaction steps. The arrow $\xrightarrow{}$ illustrates the kinetically relevant steps.

A comparison of the N_2O + CO reaction with N_2O decomposition and CO oxidation indicates as well that N_2O activation is essential to the kinetically relevant step in the reduction of N_2O by CO: The activation of CO in the kinetically relevant step of CO oxidation occurs readily at much lower temperatures than the N_2O + CO reaction[10]. It has been further reported for other Co-based TM oxides that CO activation is prevalent and N_2O is unreactive when N_2O, CO and O_2 are co-fed[22,25]. Thus, CO activation as crucial step for the N_2O + CO reaction is negated because the reaction should occur at temperatures similar to CO oxidation. In addition, the kinetically relevant step of N_2O decomposition - the associative desorption of O* - is unlikely to be relevant here because adsorbed CO* readily reacts with O* in CO oxidation. It is concluded here that N_2O +CO reaction involves N_2O activation in the kinetically relevant step on $LaCoO_3$, analogously to previous reports on other TM oxides[22].

NO + CO Reaction

Details of the NO + CO reaction on perovskite-type oxides have been subject of several studies as reviewed in ref[26]. The reduction reaction is unselective and yields N_2 or N_2O as well as the byproduct CO_2. The consecutive reaction of N_2O to N_2 is excluded from the considerations on reaction mechanism and elementary steps in this work (Eq. 6-15) because the NO + CO reaction rates were analyzed at 523 K and no significant conversion (< 5 %) were measured in N_2O decomposition and the reduction of N_2O by CO below 573 K on any catalyst in this work. The presence of strongly adsorbing NO further lowers N_2O conversion during the NO + CO reaction[27,28]. It should be noted, however, that the consecutive reaction needs to be considered at elevated temperatures and causes a shift towards N_2 selectivity with increasing temperature as reported in several studies[26]. Furthermore, isocyanate (NCO^-) surface species are unreactive in the reactions conditions[29]. As a result, the reaction of two adsorbed N atoms (Eq. 12) remains the only N_2 formation pathway under the applied reaction conditions, which occurs in parallel to the formation of N_2O from N* and NO* (Eq. 11). The disproportionation reaction of two NO molecules is a separate pathway to form N_2O (Eq. 8).

$$CO + * \overset{K_{CO}}{\rightleftharpoons} CO* \quad (6)$$

$$NO + * \overset{K_{NO}}{\rightleftharpoons} NO* \quad (7)$$

$$NO* + NO* \xrightarrow{k_0} O* + N_2O* \quad (8)$$

$$NO* + * \xrightarrow{k_1} O* + N* \quad (9)$$

$$CO* + NO* \xrightarrow{k_2} N* + CO_2* \quad (10)$$

$$N* + NO* \xrightarrow{k_3} N_2O* + * \quad (11)$$

$$N* + N* \xrightarrow{k_4} N_2 + 2* \quad (12)$$

$$CO* + O* \xrightarrow{k_5} CO_2* + * \quad (13)$$

$$CO_2* \overset{K_{CO_2}}{\rightleftharpoons} CO_2 + * \quad (14)$$

$$N_2O* \overset{K_{N_2O}}{\rightleftharpoons} N_2O + * \quad (15)$$

Scheme S2 Elementary steps of the NO + CO reaction. The arrow $\rightleftharpoons$ signals the quasi-equilibration of a reaction step.

The following considerations on the reaction mechanism discuss the selectivity and reaction rate data in the NO + CO reaction on $LaCoO_3$. The analysis of NO activation rates considers a correction by selectivity data, which ensures that NO activation rate does not account for NO molecules that react in other reaction steps than the kinetically relevant step, particularly the reaction of N* + NO* to form N_2O.

The reaction rates and selectivity are assessed as a function of reactant partial pressure and selectivity is presented as the ratio of N_2O and N_2 formation rates.

An increase in N_2O partial pressure induces only little changes on both reaction rates and selectivity (Figure 13a and b), while the effects of NO and CO partial pressure behave inversely to each other and are vastly more pronounced. Reaction rates and selectivity towards N_2 increases with rising CO partial pressure. An increased CO:NO feed ratio is therefore an option to simultaneously improve the reaction rate and desired selectivity towards N_2.

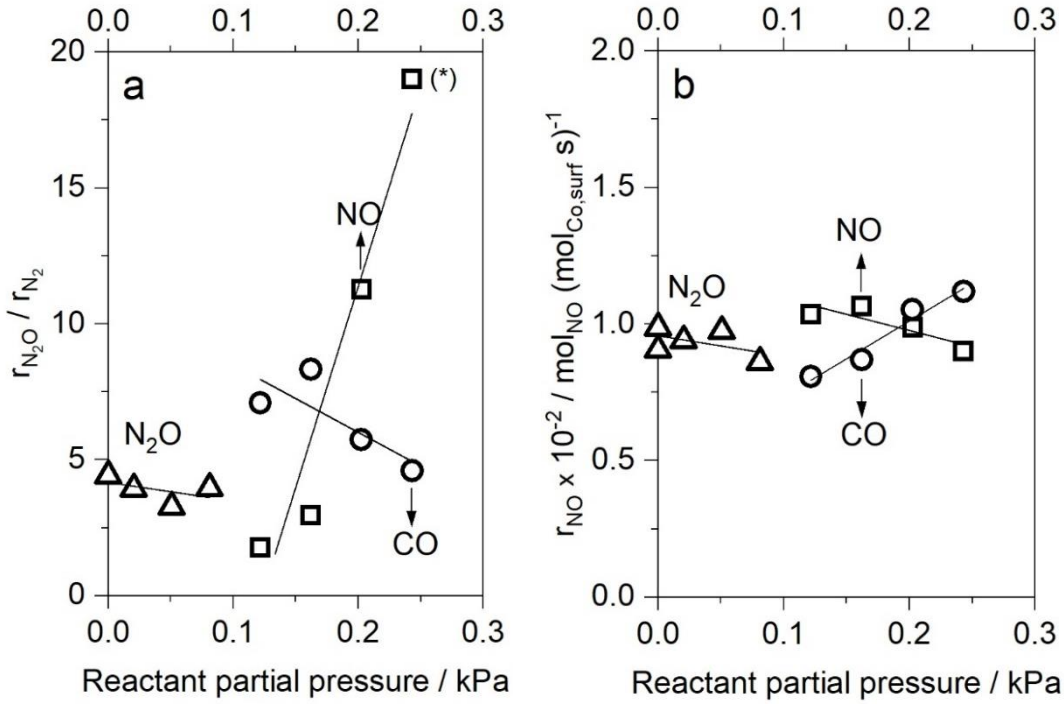

Figure S13 Effect of reactant partial pressures on the catalytic efficacy in the NO + CO reaction. Variation of **a)** selectivity as ratio of N_2O and N_2 formation rates at 523 K and **b)** NO reaction rate at 516 K with reactant and product partial pressures. ***)** N_2O selectivity just above 100% was measured for this data point. The ratio was set to a value of 19, reflecting an estimated 5 % measurement uncertainty in selectivity data. The lines in both graphs are a linear least squares fit to represent the general trend of the data.

The NO activation mechanism has been discussed with the NO dissociation (Eq. 9) as kinetically relevant step on TM-based perovskite-type oxides[26,28]. A bimolecular reaction route, which involves the surface reaction of two NO molecules (Eq. 8) or NO and CO (Eq. 10), is less discussed in literature on perovskite-type oxides. In the following, each of the three reaction steps, i.e. NO + NO disproportionation reaction, NO dissociation and NO + CO reaction, is considered as potentially kinetically-relevant in separate models and are qualitatively assessed regarding the measured effects of reactant partial pressures on reaction rates and selectivity. The surface reaction of CO* and O* is the kinetically relevant step of CO oxidation and occurs readily at lower temperatures than the NO + CO reaction and is thus not considered as possible kinetically relevant step.

The rate equations as derived from the respective kinetically relevant step and the corresponding expressions for the selectivity ratio are given in Table S2 as a function of NO (P_{NO}) and CO (P_{CO}) partial pressures. Their derivation, in which both NO and CO were assumed as the most abundant surface intermediates, is elaborated in Supplementary Note 12. It should also be noted that the assumed mechanism of NO activation affects the necessary correction for

reaction rates (see Methods & Materials section) as well as equations derived for the selectivity ratio in terms of steady state concentration of N* on the surface (Supplementary Note 13).

The disproportionation reaction of two NO* molecules yields N_2O as a product, and thus provides no pathway to significant N_2 formation because N_2O is unreactive in the conditions applied in this work. Therefore, the NO* + NO* disproportionation route with subsequent CO* + O* reaction (Pathway A) cannot be the main or sole pathway towards overall product formation. It may, however, contribute as a minor pathway towards N_2O formation.

The change in reaction rates with varying P_{NO} and P_{CO} (Figure 13b) may be described by the equation (Table S2) related to pathway C with the NO + CO surface reaction as kinetically relevant step, when the reactant partial pressure dependence is predominantly determined by the ratio in the numerator. In contrast, the equation based on the NO dissociation (pathway B) predicts lower reaction rates with increasing P_{CO}- in disagreement with experimental results. Similarly, the experimental trends in selectivity differentiate pathways B and C: N_2O selectivity increases with P_{NO} and increased P_{CO} favors N_2 formation (Figure S13a). Thus, only the equation that regards the surface reaction of NO + CO as kinetically relevant describes the trends accurately. It should be noted that pathways A and B may still contribute to the reaction rates to a minor degree, but the NO + CO reaction is concluded as the major pathway according to this analysis. The involvement of CO and NO as reactants in the kinetically relevant step is strongly indicated by the present results, but merits a full quantitative kinetic analysis to confirm and further assess details of the reaction mechanism, which is beyond the scope of this work.

It is important to note in this context that selectivity trends are subject to change at higher temperatures, when N_2O becomes reactive. In addition, the trends in reaction rates with partial pressures here are in partial disagreement with previous results at 573-673 K, where the overall reaction rate increases with both P_{NO} and P_{CO}[30,31]. Both considerations indicate a complex dependence of NO + CO kinetics on temperature. The negative order of the reaction rate in NO partial pressure at lower temperature may be the result of the higher adsorption energy of NO compared to CO[27,28]. This inhibitive impact of NO surface abundance may originate from lack of vicinal binding of NO and CO on the surface, which can be increased by higher CO partial pressure.

Table S2 Rate equations and selectivity ratios in different models of the NO + CO reactions.

Pathway A	**Pathway B**	**Pathway C**
(NO + NO)	**(NO + *)**	**(NO + CO)**

$\frac{\vec{r}_{N_2O}}{\vec{r}_{N_2}} =$	n. a.	$\frac{k_3[NO^*][N^*]}{k_4[N^*]^2} = \ldots = \frac{2}{-1+\sqrt{1+4k_1L\frac{k_4}{k_3^2K_{NO}P_{NO}(1+K_{NO}P_{NO}+K_{CO}P_{CO})}}}$	$\frac{k_3[NO^*][N^*]}{k_4[N^*]^2} = \ldots = \frac{2}{-1+\sqrt{1+4k_2\frac{k_4}{k_3^2}\frac{K_{CO}P_{CO}}{K_{NO}P_{NO}}}}$
$r_{NO} =$	$\frac{k_0}{(1+\frac{K_{CO}}{K_{NO}}\frac{P_{CO}}{P_{NO}})^2}$	$\frac{\frac{k_1}{K_{NO}P_{NO}}}{(1+\frac{K_{CO}}{K_{NO}}\frac{P_{CO}}{P_{NO}})^2}$	$\frac{k_2\frac{K_{CO}}{K_{NO}}\frac{P_{CO}}{P_{NO}}}{(1+\frac{K_{CO}}{K_{NO}}\frac{P_{CO}}{P_{NO}})^2}$

Derivation of the equations is provided in Supplementary Notes 3 and 4.

Supplementary Note 12: Derivation of Rate Equations for the Reduction of NO by CO

The Rate Equation for NO + NO as Sole Kinetically Relevant Step

Assuming that the NO* + NO* surface reaction is the kinetically relevant step leads to the following term for the numerator of the rate equation.

$$r = k_0[NO^*]^2 \tag{16}$$

The reaction involves two molecules adsorbed on vicinal active sites and requires a stochastic normalization by the total number of active species L. As the measured reaction rates are normalized by the number of active sites L, the term L^2 results in the denominator.

$$\frac{r}{L} = \frac{k_0[NO^*]^2}{L^2} \tag{17}$$

In the following, any normalized rate will be denoted as r_i for clarity. With the assumption that only NO and CO are MASI, i.e. L = [NO] + [CO], because of their strong binding to TM sites, the full rate equation is shown in Equation (20) after it is rewritten as a function of reactant partial pressures.

$$r_{NO} = \frac{k_0[NO*]^2}{([NO*]+[CO*])^2} \tag{18}$$

$$r_{NO} = \frac{k_0}{(1+\frac{[CO*]}{[NO*]})^2} \tag{19}$$

With the equilibrated adsorption of the reactants and the corresponding relations $[NO] = K_{NO}P_{NO}[*]$ and $[CO] = K_{CO}P_{CO}[*]$ follows:

$$r_{NO} = \frac{k_0}{(1+\frac{K_{CO}P_{CO}}{K_{NO}P_{NO}})^2} \tag{20}$$

The Rate Equation for NO* + * as Sole Kinetically Relevant Step

The assumption that the NO* + * surface reaction is the kinetically relevant step leads to the following term for the numerator of the rate equation.

$$r = k_1[NO*][*] \tag{21}$$

The bimolecular reaction involves two vicinal active sites and requires and requires a stochastic normalization by the number of active sites L. As the measured reaction rates are normalized by the number of active sites L, the term L^2 results in the denominator.

$$\frac{r}{L} = \frac{k_1[NO*][*]}{L^2} \tag{22}$$

In the following, any normalized rate will be denoted as r_i for clarity. With the assumption that only NO and CO are MASI, i.e. L = [NO] + [CO], because of their strong binding to TM sites, the full rate equation is shown in Equation (25) after it is rewritten as a function of reactant partial pressures.

$$r_{NO} = \frac{k_1[NO*][*]}{([NO*]+[CO*])^2} \tag{23}$$

$$r_{NO} = \frac{k_1 \frac{[*]}{[NO*]}}{(1+\frac{[CO*]}{[NO*]})^2} \tag{24}$$

With the equilibrated adsorption of the reactants and the corresponding relations $[NO] = K_{NO}P_{NO}[*]$ and $[CO] = K_{CO}P_{CO}[*]$ follows:

$$r_{NO} = \frac{\frac{k_1}{K_{NO}P_{NO}}}{(1+\frac{K_{CO}P_{CO}}{K_{NO}P_{NO}})^2} \tag{25}$$

The Rate Equation for NO* + CO* as Sole Kinetically Relevant Step

The assumption that the NO* + CO* surface reaction is the kinetically relevant step leads to the following term for the numerator of the rate equation.

$$r = k_1[NO*][CO*] \tag{26}$$

The bimolecular reaction involves two molecules adsorbed on vicinal active sites and requires and requires a stochastic normalization by the number of active sites L. As the measured reaction rates are normalized by the number of active sites L, the term L^2 results in the denominator.

$$\frac{r}{L} = \frac{k_1[NO*][CO*]}{L^2} \tag{27}$$

In the following, any normalized rate will be denoted as r_i for clarity. With the assumption that only NO and CO are MASI, i.e. L = [NO] + [CO], because of their strong binding to TM sites, the full rate equation is shown in Equation XXX and can be rewritten as a function of [CO]/[NO] ratios.

$$r_{NO} = \frac{k_1[NO*][CO*]}{([NO*]+[CO*])^2} \tag{28}$$

$$r_{NO} = \frac{k_1 \frac{[CO*]}{[NO*]}}{(1+\frac{[CO*]}{[NO*]})^2} \quad (29)$$

$$r_{NO} = \frac{k_1 \frac{K_{CO}P_{CO}}{K_{NO}P_{NO}}}{(1+\frac{K_{CO}P_{CO}}{K_{NO}P_{NO}})^2} \quad (30)$$

Supplementary Note 13: Derivation of Equations for the NO + CO Selectivity Ratio

NO* + CO* Step as Sole Kinetically Relevant Step

This section lines out equations for the selectivity in the NO + CO reaction with the assumption that the NO + NO reaction has no impact on the selectivity. The following set of reaction steps occur in the reaction system:

$$CO + * \overset{K_{CO}}{\rightleftharpoons} CO* \quad (31)$$

$$NO + * \overset{K_{NO}}{\rightleftharpoons} NO* \quad (32)$$

$$CO* + NO* \overset{k_2}{\rightarrow} N* + CO_2* \quad (33)$$

$$N* + NO* \overset{k_3}{\rightarrow} N_2O* + * \quad (34)$$

$$N* + N* \overset{k_4}{\rightarrow} N_2 + 2* \quad (35)$$

$$CO_2* \overset{K_{CO_2}}{\rightleftharpoons} CO_2 + * \quad (36)$$

$$N_2O* \overset{K_{N_2O}}{\rightleftharpoons} N_2O + * \quad (37)$$

The formation of N_2O or N_2 is thus defined by the reaction steps in Equation (34) or Equation (35), respectively, and results in the following formation rates and product formation ratio.

$$\vec{r}_{N_2O} = k_3[NO*][N*] \quad (38)$$

$$\vec{r}_{N_2} = k_4[N^*]^2 \tag{39}$$

$$\frac{\vec{r}_{N_2O}}{\vec{r}_{N_2}} = \frac{k_3[NO^*][N^*]}{k_4[N^*]^2} = \frac{k_3[NO^*]}{k_4[N^*]} \tag{40}$$

The surface concentration of NO [NO*] is defined by the equilibrated adsorption in Equation (32), while the surface concentration of N [N*] is in a steady-state equilibrium with its formation and consumption:

$$0 = k_2[NO^*][CO^*] - k_3[NO^*][N^*] - k_4[N^*]^2 \tag{41}$$

The rearrangement of Equation (41) for [N*] yields two possible solutions. Only the solution with a minus sign in front of the root, however, is physically meaningful because a negative sign yields a negative numerator as the relation $k_3[NO^*] < \sqrt{(k_3[NO^*])^2 + 4k_2k_4[NO^*][CO^*]}$ is at all times valid:

$$[N^*] = \frac{-k_3[NO^*] + \sqrt{(k_3[NO^*])^2 + 4k_2k_4[NO^*][CO^*]}}{2k_4} \tag{42}$$

After insertion of the solution for [N*], the selectivity ratio is as follows and can be rearranged to yield a clearer picture on the dependence on reactant partial pressures.

$$\frac{\vec{r}_{N_2O}}{\vec{r}_{N_2}} = \frac{k_3[NO^*]}{k_4 \dfrac{-k_3[NO^*] + \sqrt{(k_3[NO^*])^2 + 4k_2k_4[NO^*][CO^*]}}{2k_4}} \tag{43}$$

The equation can be rewritten by moving k_2, and [NO*] out of the root terms and sums in the denominator.

$$\frac{\vec{r}_{N_2O}}{\vec{r}_{N_2}} = \frac{2}{-1 + \sqrt{1 + 4k_2 \dfrac{k_4}{k_3^2} \dfrac{[CO^*]}{[NO^*]}}} \tag{44}$$

$$\frac{\vec{r}_{N_2O}}{\vec{r}_{N_2}} = \frac{2}{-1 + \sqrt{1 + 4k_2 \dfrac{k_4}{k_3^2} \dfrac{K_{CO}P_{CO}}{K_{NO}P_{NO}}}} \tag{45}$$

This result shows that r_{N2O}/r_{N2} increases with increasing NO surface concentration and with decreasing CO surface concentration, which agrees with experimental results (see Supplementary note 11). Either

NO Dissociation Reaction as Sole Kinetically Relevant Step

This section lines out equations for the selectivity in the NO + CO reaction with the assumption that the NO + NO reaction has no impact on the selectivity. The following set of reaction steps occur in the reaction system:

$$CO + * \overset{K_{CO}}{\rightleftharpoons} CO* \tag{46}$$

$$NO + * \overset{K_{NO}}{\rightleftharpoons} NO* \tag{47}$$

$$NO* + * \overset{k_1}{\rightarrow} N* + O* \tag{48}$$

$$N* + NO* \overset{k_3}{\rightarrow} N_2O* + * \tag{49}$$

$$N* + N* \overset{k_4}{\rightarrow} N_2 + 2* \tag{50}$$

$$CO_2* \overset{K_{CO_2}}{\rightleftharpoons} CO_2 + * \tag{51}$$

$$N_2O* \overset{K_{N_2O}}{\rightleftharpoons} N_2O + * \tag{52}$$

The formation of N_2O or N_2 is thus defined by the reaction steps in Equation (34) or Equation (35), respectively, and results in the following formation rates and product formation ratio.

$$\vec{r}_{N_2O} = k_3[NO*][N*] \tag{53}$$

$$\vec{r}_{N_2} = k_4[N*]^2 \tag{54}$$

$$\frac{\vec{r}_{N_2O}}{\vec{r}_{N_2}} = \frac{k_3[NO*][N*]}{k_4[N*]^2} = \frac{k_3[NO*]}{k_4[N*]} \tag{55}$$

The surface concentration of NO [NO*] is defined by the equilibrated adsorption in Equation (32), while the surface concentration of N [N*] is in a steady-state equilibrium with its formation and consumption:

$$0 = k_1[NO*][*] - k_3[NO*][N*] - k_4[N*]^2 \tag{56}$$

$$[*] = \frac{L}{1 + K_{NO}P_{NO} + K_{CO}P_{CO}} \tag{57}$$

$$0 = \frac{k_1[NO^*]L}{1 + K_{NO}P_{NO} + K_{CO}P_{CO}} - k_3[NO^*][N^*] - k_4[N^*]^2 \tag{58}$$

The rearrangement of Equation (41) for [N*] yields two possible solutions. Only the solution with a minus sign in front of the root, however, is physically meaningful because a negative sign yields a negative numerator as the relation $k_3[NO^*] < \sqrt{(k_3[NO^*])^2 + 4k_1k_4L\frac{[NO^*]}{1 + K_{NO}P_{NO} + K_{CO}P_{CO}}}$ is at all times valid:

$$[N^*] = \frac{-k_3[NO^*] + \sqrt{(k_3[NO^*])^2 + 4k_1k_4L\frac{[NO^*]}{1 + K_{NO}P_{NO} + K_{CO}P_{CO}}}}{2k_4} \tag{59}$$

After insertion of the solution for [N*], the selectivity ratio is as follows and can be rearranged to yield a clearer picture on the dependence on reactant partial pressures.

$$\frac{\vec{r}_{N_2O}}{\vec{r}_{N_2}} = \frac{k_3[NO^*]}{k_4\frac{-k_3[NO^*] + \sqrt{(k_3[NO^*])^2 + 4k_1k_4L\frac{[NO^*]}{1 + K_{NO}P_{NO} + K_{CO}P_{CO}}}}{2k_4}} \tag{60}$$

The equation can be rewritten by moving k_2, and [NO*] out of the root terms and sums in the denominator.

$$\frac{\vec{r}_{N_2O}}{\vec{r}_{N_2}} = \frac{2}{-1 + \sqrt{1 + 4k_1L\frac{k_4}{k_3^2[NO^*](1 + K_{NO}P_{NO} + K_{CO}P_{CO})}}} \tag{61}$$

$$\frac{\vec{r}_{N_2O}}{\vec{r}_{N_2}} = \frac{2}{-1 + \sqrt{1 + 4k_1L\frac{k_4}{k_3^2K_{NO}P_{NO}(1 + K_{NO}P_{NO} + K_{CO}P_{CO})}}} \tag{62}$$

This result implies that in this case r_{N2O}/r_{N2} would increase with increasing NO surface concentration and with increasing CO surface concentration, which is in contrast to the experimental results (see Supplementary note 11).

Supplementary Note 14: Details on gases used in reaction measurements chemocatalytic experiments

Table S3 Details on on gases used in reaction measurements.

	Reactant gases			Inert Gases		
Gas	NO	CO	N_2O	He	Ar	N_2
Concentration in gas cylinder / % (Purity)	1.0 (2.0)	1.0 (2.8)	1.0 (2.5)	100 (5.0)	100 (4.8)	100 (5.0)
Supplier*	Wf	Pr	Pr	Pr	Wf	Wf

*Gas suppliers were Westfalen GmbH (Wf) and Praxair (Pr).

References

[1] R. Jacobs, J. Booske, D. Morgan, R. Jacobs, D. Morgan, J. Booske, *Adv. Funct. Mater.* **2016**, *26*, 5471–5482.

[2] J. Chen, X. Wu, A. Selloni, **2011**, *83*, 245204.

[3] B. M. Weiss, N. Artioli, E. Iglesia, *ChemCatChem* **2012**, *4*, 1397–1404.

[4] R. P. Vasquez, A. Phys Lett, *Surf. Sci. Spectra* **1992**, *1*, DOI 10.1116/1.1247633.

[5] M. Krzywiecki, L. Grządziel, A. Sarfraz, D. Iqbal, A. Szwajca, A. Erbe, *Phys. Chem. Chem. Phys.* **2015**, *17*, 10004–10013.

[6] F. M. F. De Groot, M. Grioni, J. C. Fuggle, J. Ghijsen, G. A. Sawatzky, H. Petersen, *Phys. Rev. B* **1989**, *40*, 5715.

[7] J. Suntivich, W. T. Hong, Y. L. Lee, J. M. Rondinelli, W. Yang, J. B. Goodenough, B. Dabrowski, J. W. Freeland, Y. Shao-Horn, *J. Phys. Chem. C* **2014**, *118*, 1856–1863.

[8] M. Abbate, R. Potze, G. A. Sawatzky, A. Fujimori, *Phys. Rev. B* **1994**, *49*, 7210.

[9] W. T. Hong, K. A. Stoerzinger, B. Moritz, T. P. Devereaux, W. Yang, Y. Shao-Horn, *J. Phys. Chem. C* **2015**, *119*, 2063–2072.

[10] J. Simböck, M. Ghiasi, S. Schönebaum, U. Simon, F. M. F. de Groot, R. Palkovits, *Nat. Commun.* **2020**, *11*, 1–10.

[11] N. Palina, A. Annadi, T. C. Asmara, C. Diao, X. Yu, M. B. H. Breese, T. Venkatesan, Ariando, A. Rusydi, *Phys. Chem. Chem. Phys.* **2016**, *18*, 13844–13851.

[12] C. Wang, L. Zeng, W. Guo, C. Gong, J. Yang, *RSC Adv.* **2019**, *9*, 35646–35654.

[13] P. V. B. Santiago, C. C. Lima, J. L. Bott-Neto, P. S. Fernández, C. A. Angelucci, J. Souza-Garcia, *J. Electroanal. Chem.* **2021**, *896*, 115198.

[14] J. Suntivich, K. J. May, H. A. Gasteiger, J. B. Goodenough, Y. Shao-Horn, *Science (80-.).* **2011**, *334*, 1383–1385.

[15] A. Grimaud, O. Diaz-Morales, B. Han, W. T. Hong, Y. L. Lee, L. Giordano, K. A. Stoerzinger, M. T. M. Koper, Y. Shao-Horn, *Nat. Chem. 2017 95* **2017**, *9*, 457–465.

[16] W. T. Hong, K. A. Stoerzinger, Y. L. Lee, L. Giordano, A. Grimaud, A. M. Johnson, J. Hwang, E. J. Crumlin, W. Yang, Y. Shao-Horn, *Energy Environ. Sci.* **2017**, *10*, 2190–2200.

[17] D. N. Mueller, M. L. MacHala, H. Bluhm, W. C. Chueh, *Nat. Commun. 2015 61* **2015**, *6*, 1–8.

[18] J. T. Mefford, X. Rong, A. M. Abakumov, W. G. Hardin, S. Dai, A. M. Kolpak, K. P. Johnston, K. J. Stevenson, *Nat. Commun. 2016 71* **2016**, *7*, 1–11.

[19] C. C. L. McCrory, S. Jung, J. C. Peters, T. F. Jaramillo, *J. Am. Chem. Soc.* **2013**, *135*, 16977–16987.

[20] D. M. Morales, M. Risch, *J. Phys. Energy* **2021**, *3*, 034013.

[21] B. Izadkhah, A. Niaei, M. J. Illán-Gómez, D. Salari, A. Tarjomannejad, V. Albaladejo-Fuentes, *Ind. Eng. Chem. Res.* **2017**, *56*, 3880–3886.

[22] K. Pacultová, L. Obalová, F. Kovanda, K. Jirátová, *Catal. Today* **2008**, *137*, 385–389.

[23] K. S. Chang, X. Peng, *J. Ind. Eng. Chem.* **2010**, *16*, 455–460.

[24] R. Sundararajan, V. Srinivasan, *Appl. Catal. A Gen.* **1996**, *141*, 45–56.

[25] K. S. Chang, H. J. Lee, Y. S. Park, J. W. Woo, *Appl. Catal. A Gen.* **2006**, *309*, 129–138.

[26] S. Royer, D. Duprez, F. Can, X. Courtois, C. Batiot-Dupeyrat, S. Laassiri, H. Alamdari, *Chem. Rev.* **2014**, *114*, 10292–10368.

[27] A. A. Leontiou, A. K. Ladavos, G. S. Armatas, P. N. Trikalitis, P. J. Pomonis, *Appl. Catal. A Gen.* **2004**, *263*, 227–239.

[28] R. Zhang, A. Villanueva, H. Alamdari, S. Kaliaguine, *J. Mol. Catal. A Chem.* **2006**, *258*, 22–34.

[29] L. Forni, C. Oliva, T. Barzetti, E. Selli, A. M. Ezerets, A. V. Vishniakov, *Appl. Catal. B Environ.* **1997**, *13*, 35–43.

[30] N. Mizuno, M. Tanaka, M. Misono, *J. Chem. Soc. Faraday Trans.* **1992**, *88*, 91–95.

[31] N. Mizuno, M. Yamatcv, M. Tanaka, M. Misono, *Chem. Mater.* **1989**, *1*, 232–236.